

Article

A Density Functional Tight Binding Study of Acetic Acid Adsorption on Crystalline and Amorphous Surfaces of Titania

Sergei Manzhos^{1,*}, Giacomo Giorgi^{2,3} and Koichi Yamashita^{2,3}

¹ Department of Mechanical Engineering, National University of Singapore, Block EA #07-08, 9 Engineering Drive 1, Singapore 117576, Singapore

² Department of Chemical System Engineering, School of Engineering, University of Tokyo, 7-3-1, Hongo, Bunkyo-ku, Tokyo 113-8656, Japan; E-Mails: giacomo@tcl.t.u-tokyo.ac.jp (G.G.); yamasita@chemsys.t.u-tokyo.ac.jp (K.Y.)

³ CREST-JST, 7 Gobancho, Chiyoda-ku, Tokyo 102-0076, Japan

* Author to whom correspondence should be addressed; E-Mail: mpemanzh@nus.edu.sg; Tel.: +65-6516-4605; Fax: +65-6779-1459.

Academic Editor: Derek J. McPhee

Received: 4 January 2015 / Accepted: 13 February 2015 / Published: 17 February 2015

Abstract: We present a comparative density functional tight binding study of an organic molecule attachment to TiO₂ via a carboxylic group, with the example of acetic acid. For the first time, binding to low-energy surfaces of crystalline anatase (101), rutile (110) and (B)-TiO₂ (001), as well as to the surface of amorphous (*a*-) TiO₂ is compared with the same computational setup. On all surfaces, bidentate configurations are identified as providing the strongest adsorption energy, $E_{ads} = -1.93$, -2.49 and -1.09 eV for anatase, rutile and (B)-TiO₂, respectively. For monodentate configurations, the strongest $E_{ads} = -1.06$, -1.11 and -0.86 eV for anatase, rutile and (B)-TiO₂, respectively. Multiple monodentate and bidentate configurations are identified on *a*-TiO₂ with a distribution of adsorption energies and with the lowest energy configuration having stronger bonding than that of the crystalline counterparts, with E_{ads} up to -4.92 eV for bidentate and -1.83 eV for monodentate adsorption. Amorphous TiO₂ can therefore be used to achieve strong anchoring of organic molecules, such as dyes, that bind via a -COOH group. While the presence of the surface leads to a contraction of the band gap vs. the bulk, molecular adsorption caused no appreciable effect on the band structure around the gap in any of the systems.

Keywords: titanium dioxide; anatase; rutile; (B)-TiO₂; amorphous TiO₂; acetic acid; adsorption; dye-sensitized solar cells; density functional tight binding

1. Introduction

Titanium oxide is widely used in various electrochemical technologies, namely heterogeneous catalysis and photocatalysis [1,2], fuel cells [3,4], solar cells (dye-sensitized, DSSC [5–9], and perovskite-sensitized, PSSC [10,11]) and electrochemical batteries [12–18]. It is relatively abundant, inexpensive, safe and possesses a band structure suitable for these electrochemical and photocatalytic applications [19]. The three most stable phases are usually employed: anatase, rutile and (B). In all of these applications, molecules interact with titania surfaces. While some higher-energy, higher-index surfaces are sometimes explored [20,21], most applications have relied on low-energy anatase (101), rutile (110) and (B) (001) surfaces [1,2,22–24], which is justified by the ease of synthesis and stability.

In the applications in DSSC anodes, as well as in studies of carboxylic acids on TiO₂, molecules typically bind to TiO₂ via the -COOH group, with bidentate bridging and monodentate configurations dominating [9,25–30]. Bidentate chelating configurations are sometimes considered, but are usually much less stable [9,25,31,32]. Adsorption of organic molecules via a carboxylic moiety is also important for other applications. For example, the 21 amino acids possess the -COOH group, which plays a role in adsorption on TiO₂. These interactions are of interest for the development of biocompatible and bio-inspired nanostructured materials [33]. A key parameter of the interaction of molecules with TiO₂ surfaces is binding strength. It controls the stability of DSSC anodes, as well as the degree of electronic coupling, which directly influences the electron transfer rate [26,34]. It also controls the reaction rates in catalytic applications [1,2]. The ability to control or to strengthen binding by the choice of a specific TiO₂ surface is therefore important in all of these applications.

Applications of these crystalline phases and surfaces have also been supported by extensive theoretical and computational studies [35–39] and, specifically, studies of molecular adsorption via the carboxylic group onto selected crystalline phases [9,25–29,31,32]. Amorphous titania (*a*-TiO₂) has recently attracted interest for its use in the dye-sensitized technology [40–42], as well as in electrochemical batteries [43–48] and in photocatalysis [49]. These studies indicate that *a*-TiO₂ may be advantageous in these applications for several reasons. For example, the rate capability of battery electrodes made of nanostructured amorphous TiO₂ was found to be higher than that of nanostructured anatase TiO₂ due to the higher Li-diffusion coefficient in amorphous TiO₂ [44,47]. *a*-TiO₂ has also been shown to possess a distribution of binding energies to Li, Na and Mg, with the lowest binding energy stronger than that of the anatase, rutile and (B) phases [50,51]. The same might hold for molecular adsorption and needs to be quantified. The presence of amorphous TiO₂ in the anodes of DSSC has been shown to improve conversion efficiency [42]. Low-crystallinity TiO₂ DSSC anodes have shown a high open circuit voltage and low recombination [41]. *a*-TiO₂ could also be a cheaper alternative to crystalline phases for photocatalytic applications, as it possesses similar band gap characteristics to anatase [49,52].

There are still few computational studies of the properties of *a*-TiO₂ relevant for these applications [40,49–53]. Specifically, there are no *ab initio* studies comparing at the same level of theory and with the same computational parameters the adsorption of organic molecules on the surfaces of all of the phases of TiO₂ that are finding use in electrochemical technologies, *i.e.*, anatase, rutile, (B) and amorphous. As *ab initio* methods still possess only semi-quantitative accuracy, results obtained with different phases in different studies using different computational setups are not directly comparable. Here, we present a study that compares with the same computational setup the adsorption of a prototypical organic molecule endowed with a -COOH anchoring group (acetic acid) to low energy crystalline surfaces, namely, anatase (101), rutile (110) and (B) (001), and to amorphous surfaces. We therefore aim to compare for the first time the adsorption modes among different phases and to understand the effect of amorphization on the geometries and binding strength of molecules.

2. Theoretical and Computational Methods

Calculations were performed using the self-consistent charge density functional tight binding scheme (SCC-DFTB) [54] and the DFTB + code [55]. SCC-DFTB is an approximate DFT approach derived from a second-order expansion of the DFT energy with respect to charge density fluctuations and provides *ab initio* accuracy for systems for which it is parameterized. We used the parameter set (Slater–Koster files) “matsci-0-3”, which has been benchmarked, in particular, for TiO₂ and for organic molecules interacting with TiO₂ [56].

For bulk TiO₂ calculations, we used conventional standard cells with 4, 2 and 8 formula units for anatase, rutile and (B), respectively. The Brillouin zone was sampled with a *k*-point density no less than one point per 30⁻¹ Å⁻¹. Converged results were obtained with 10 × 10 × 5, 8 × 8 × 12, and 3 × 10 × 6 *k*-points for anatase, rutile and (B), respectively. The initial structure of *a*-TiO₂ was taken from [52] and re-optimized within the present setup. A 192-atom supercell of a size of about 13 × 13 × 13 Å was used, and converged results were obtained with 3 × 3 × 3 *k*-points.

Anatase (101), rutile (110) and B (001) low-energy surfaces were modeled with slabs of a thickness of at least 13 Å, which are shown in Figures 2–4. The lateral (*xy*) extent of the supercell was about 10.5 × 11.5 Å, 12 × 13 Å and 12.5 × 11.3 Å, for anatase, rutile and (B), respectively. The top half of the slab (in the *z* direction) was optimized, and the bottom half held at bulk positions during optimization. The amorphous surfaces were obtained from the bulk supercell by adding a vacuum in the *z* direction. Two surfaces were obtained by optimizing the top/bottom half and fixing the bottom/top half of the slab; these are labeled as “top” and “bottom” surfaces. This is a similar approach to that used in [53]. All surface supercells were 30 Å in the *z* direction, and 3 × 3 × 1 *k*-points were used. Acetic acid molecules were then positioned above the surfaces in various configurations with the COOH group in monodentate or bidentate binding to the surface and optimized with DFTB. We here focus on bidentate binding in bridging configurations, which are known to be much more stable than chelating configurations [9,25,31,32].

The adsorption energy (E_{ads}) of AcOH on top of all of the surfaces here considered has been calculated as:

$$E_{ads} = E_{surf + AcOH} - (E_{surf} + E_{AcOH}) \quad (1)$$

where E_{surf} , E_{AcOH} and $E_{surf + AcOH}$ represent the energy of, respectively, the optimized surface, a free optimized acetic acid molecule and of the final optimized anchored system formed by the surface and acetic acid.

3. Results and Discussion

3.1. TiO_2 Bulk and Surfaces

Anatase: The cell vectors of the optimized bulk anatase (conventional standard cell) are $a = b = 3.81 \text{ \AA}$, $c = 9.73 \text{ \AA}$, in good agreement with previously reported experimental and computed values [57–61]. The energy per formula unit is -215.181 eV . The density of states is shown in Figure 1 and shows a band gap of about 3.2 eV , in good agreement with experimental values of $3.2\text{--}3.3 \text{ eV}$ [62] and prior DFTB calculations [63]. The presence of the (101) surface causes a contraction of the band gap by about 0.5 eV .

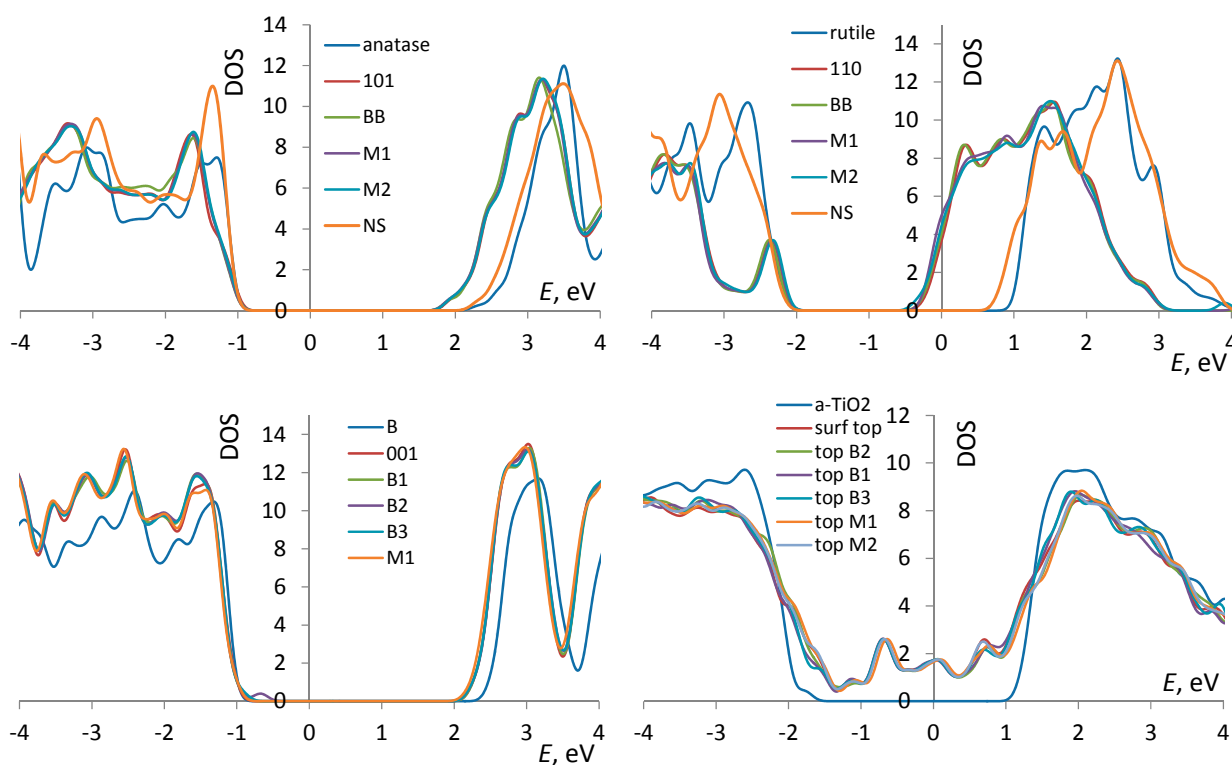


Figure 1. The densities of states (DOSs) of bulk anatase, rutile, (B) and a - TiO_2 and their surfaces, as well as surfaces with AcOH adsorbed in different configurations (described in Section 3.1). For each phase, the zero of the energy axis corresponds to the Fermi energy in the bulk, and the DOSs of surfaces are plotted to match the valence band maximum. Gaussian broadening of 0.1 eV . For a - TiO_2 , only the “top” surface data are shown. The curves for the “bottom” surface are qualitatively similar. For (B)- TiO_2 and a - TiO_2 , curves for the selected adsorption configurations are shown; the curves for other adsorption configurations are similar. For anatase and rutile, the DOSs for nanosheets (“NS”) are also shown.

Rutile: The cell vectors of the optimized rutile phase are $a = b = 4.61 \text{ \AA}$, $c = 2.97 \text{ \AA}$, in good agreement with previously reported values [57,58,61]. The density of states is shown in Figure 1 and shows a band gap of about 3.1 eV, in good agreement with reported values of about 3 eV [22,64–66] and consistent with that of anatase. The energy per formula unit is -215.481 eV . The calculations therefore correctly reproduce the anatase-rutile phase ordering, albeit with a difference of 0.1 eV per atom, which is higher than the reported values of 0.012–0.015 eV [67,68]. This, however, is not critical for the present purpose of studying molecular adsorption. This accuracy is also comparable with that of previously reported DFT values for cohesive energies ranging from -18.77 to -21.44 eV [69,70] for rutile and from -21.54 to -21.60 eV [70,71] for anatase. The presence of the interface ((110) surface) causes a contraction of the band gap by about 1.5 eV.

(B): The cell parameters of the optimized (B) phase are $a = 12.45 \text{ \AA}$, $b = 3.76 \text{ \AA}$, $c = 6.69 \text{ \AA}$, $\alpha = \gamma = 90^\circ$, $\beta = 107.3^\circ$, in good agreement with previously reported values [22,72]. The density of states is also shown in Figure 1 and shows a band gap of about 3.1 eV, in good agreement with the experimental value of 3.2 eV [73]. The energy per formula unit is -215.365 eV , *i.e.*, similar to previous *ab initio* calculations, we obtain that (B) is more stable than anatase, although this is in contradiction with the low abundance of (B) relative to anatase and rutile [22,57]. The effect of the (001) surface on the band structure is the least significant among the three crystalline phases, decreasing the band gap by about 0.3 eV. This can be rationalized by the low surface energy of this surface [22], as well as by the substantial slab thickness we used (6 Ti layers *vs.* 4 Ti layers for the rutile (110) slab, which shows the strongest effect of the surface on the gap; see Figures 2–4).

a-TiO₂: The optimization in DFTB+ resulted in some atomic relaxation, but largely preserved the original structure of [52]. The energy per formula unit is -214.795 eV , *i.e.*, metastability by about 0.13 eV per atom *vs.* anatase, similar to that reported in [52]. The density of states shown in Figure 1 for bulk *a*-TiO₂ shows a similar gap of about 3 eV to that of the crystalline phases, similar to the report of [52]. The introduction of the surface gives rise to multiple states in the band gap, also shown in Figure 1.

The reduction of the bandgap is partly due to the limited thickness of the slab and the fixation of the bottom layers. The reduction is much less severe if all atoms are allowed to relax (*i.e.*, a nanosheet model), as shown in Figure 1 for anatase and rutile (orange lines). We have also performed a plane wave DFT calculation on the same slab of anatase (surface and nanosheet) using the Vienna *ab initio* simulation package (VASP) code [74–77], the PBE functional [78], PAW pseudopotentials [79] and a cutoff energy of 600 eV and confirmed that the same effect is observed. Similar to DFTB results, no significant effect on the densities of state (DOS) of molecular adsorption was observed.

3.2. Adsorption Configurations of AcOH and Energetics

Anatase (101): Similar to previous works [31,80], a bidentate (BB) and two monodentate configurations (M1 and M2) were identified. These are shown in Figure 2, and their adsorption energies are listed in Table 1. The BB mode is therefore preferred. In the bidentate configuration, both oxygen atoms of the carboxylic group bind to surface Ti atoms with both O_{mol}-Ti bonds equal to 2.22 Å. The H atom is dissociated from the molecule and is bound to a surface oxygen. In the monodentate configurations, the molecules are undissociated, with O_{mol}-Ti bonds of 2.26 Å and hydrogen bonds between the H atom and a surface oxygen of 1.62 Å, in both M1 and M2 configurations. Molecular

adsorption has no appreciable effect on the band structure around the gap regardless of the configuration (Figure 1).

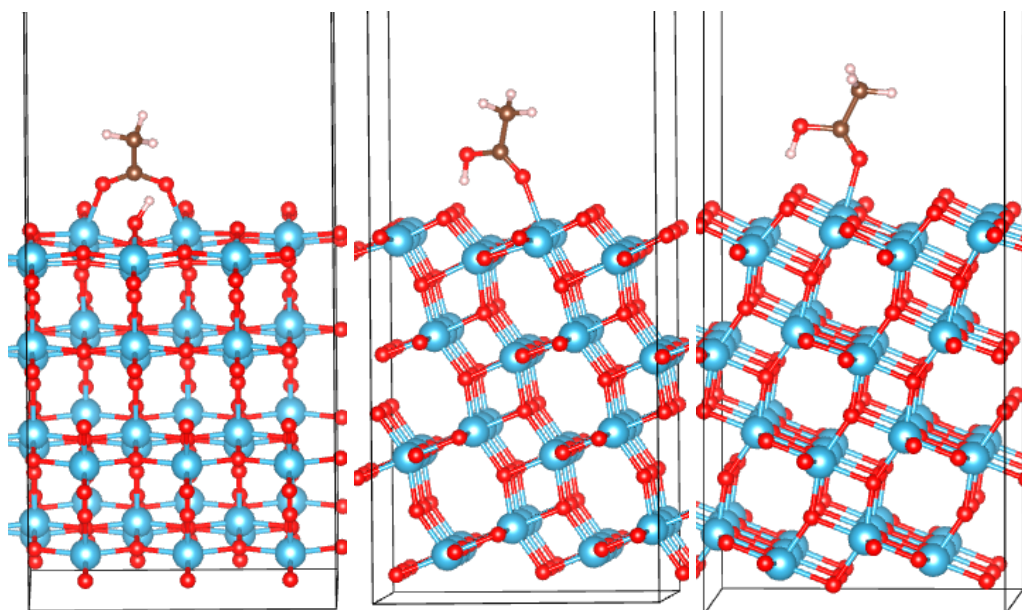


Figure 2. Adsorption configurations of AcOH on the anatase (101) surface of TiO₂: bidentate (BB) (left), M1 (monodentate) (middle) and M2 (right). The atom color code here and elsewhere: Ti, blue; O, red; C, brown; H, light grey. Visualization here and elsewhere by VESTA [87].

For AcOH on anatase (101), we can compare the adsorption energies computed with DFTB (Table 1) to previous DFT calculations. Using the SIESTA code [81], the PBE functional [78], broad DZP basis functions and Troullier–Martins pseudopotentials [82], Chan *et al.* computed E_{ads} of -1.71 , -1.56 and -1.50 eV for the BB, M1 and M2 configurations, respectively, using a thinner slab than in the present study [80]. Spreafico *et al.* [30] computed E_{ads} values of -1.25 and -1.27 eV for the BB and M1 configurations, respectively, by using the CP2K code [83], the PBE functional, Goedecker pseudopotentials [84], a mixed Gaussian-plane wave (GPW) basis [85], also employing the dispersion correction scheme of Grimme [86]. The values were also dependent on slab size [30]. In [31], the adsorption strength of the M1, M2 and BB modes was compared with different DFT setups, including a cluster of slab TiO₂ models, localized or plane wave basis functions and GGA or hybrid functionals. The stability of M1 and M2 relative to BB was ± 0.5 eV [31]. We have also made a plane-wave DFT calculation with VASP [74–77], using the PBE functional, PAW pseudopotentials [79] and a plane wave cutoff of 600 eV. We obtained E_{ads} values of -0.91 , -0.95 and -0.91 eV for M1, M2 and BB configurations, respectively. The differences in the values of E_{ads} of the order of half an eV observed among different commonly accepted DFT setups, including differences of the order of 0.5 eV in relative E_{ads} for different adsorption configurations, highlight the need to use one and the same setup to obtain truly comparative values of E_{ads} among different phases and configurations. Interestingly, a measured infrared spectrum of AcOH on the anatase (101) surface pointed to bidentate adsorption [31].

Table 1. Adsorption energies E_{ads} of AcOH in different configurations on anatase (101), rutile (110) and (B) (001) surfaces of TiO_2 , as well as on two amorphous surfaces. The bond length for bonding between the molecule's and surface atoms, as well as charges on the molecule q are also given. For bidentate configurations, the two bond lengths are $O_{\text{mol-Ti}}$; for monodentate, they are $O_{\text{mol-Ti}}$ and $H-O_{\text{surf}}$.

System	E_{ads} , eV	q , e	$O_{\text{mol-Ti}}$, Å	$O_{\text{mol-Ti/H-O}_{\text{surf}}}$, Å
Anatase (101)				
BB	−1.93	−0.12	2.22	2.22
M1	−0.93	0.16	2.26	1.62
M2	−1.06	0.17	2.26	1.62
Rutile (110)				
BB	−2.49	−0.11	2.21	2.21
M1	−1.04	0.17	2.26	1.60
M2B	−1.11	0.34	2.27	2.29
B (001)				
BB1	−0.74	−0.17	2.24	2.25
BB2	−0.41	−0.18	2.25	2.25
BB3	−1.07	−0.16	2.23	2.24
M1	−0.78	0.17	2.27	1.83
M2	−0.79	0.18	2.27	1.87
M3	−0.86	0.19	2.27	1.97
M4	−0.70	0.17	2.27	1.87
M5	−0.79	0.19	2.27	2.08
M6	−0.75	0.18	2.27	1.86
α - TiO_2				
top BB1	−2.60	0.03	1.93	2.25
top BB2	−3.56	0.00	1.94	2.24
top BB3	−2.96	−0.03	1.93	2.27
top M1	−2.20	0.33	1.96	1.60
top M2	−2.40	0.35	1.95	1.60
top M3	−2.38	0.35	1.95	1.63
top M4	−0.97	0.18	2.26	1.63
top M5	−0.80	0.16	2.26	1.62
bottom BB1	−4.43	0.04	1.91	1.95
bottom BB2	−4.92	0.08	1.97	2.00
bottom BB3	−0.28	−0.07	2.21	2.22
bottom M1	−1.18	0.18	2.25	1.69
bottom M2	−0.84	0.14	2.25	1.63
bottom M3	−1.53	0.19	2.23	1.62
bottom M4	−1.83	0.14	1.93	1.77

Rutile (110): Two bidentate (BB and M2B) and a monodentate configuration (M1) are identified. These are shown in Figure 3, and their adsorption energies are listed in Table 1. In the bidentate BB configuration, both oxygen atoms of the carboxylic group bind to surface Ti atoms with both $O_{\text{mol-Ti}}$ bonds equal to 2.21 Å. The H atom is dissociated from the molecule and is bound to a surface oxygen.

In the monodentate configuration (M1), the molecule is undissociated, with $O_{\text{mol-Ti}}$ bonds of 2.26 Å and hydrogen bonds between the H atom and a surface oxygen of 1.60 Å. The configuration M2B was attempted as a monodentate configuration, where the molecular hydrogen coordinates to an in-plane oxygen atom of TiO_2 . This configuration, however, converged to a bidentate configuration in which AcOH preserves the H atom and in which a hydrogen atom of the CH_3 group is 2.21 Å away from a surface O atom. This configuration is less stable than the dissociated bidentate configuration by more than 1 eV and has larger $O_{\text{mol-Ti}}$ bond lengths (2.27 and 2.29 Å) than the dissociated configuration. Similar to anatase, molecular adsorption has no appreciable effect on the band structure regardless of the configuration (Figure 1). The energetic preference of AcOH for bidentate configurations computed here (Table 1) is in agreement with known preference for bidentate bridging adsorption on the clean (110) surface identified experimentally [88,89].

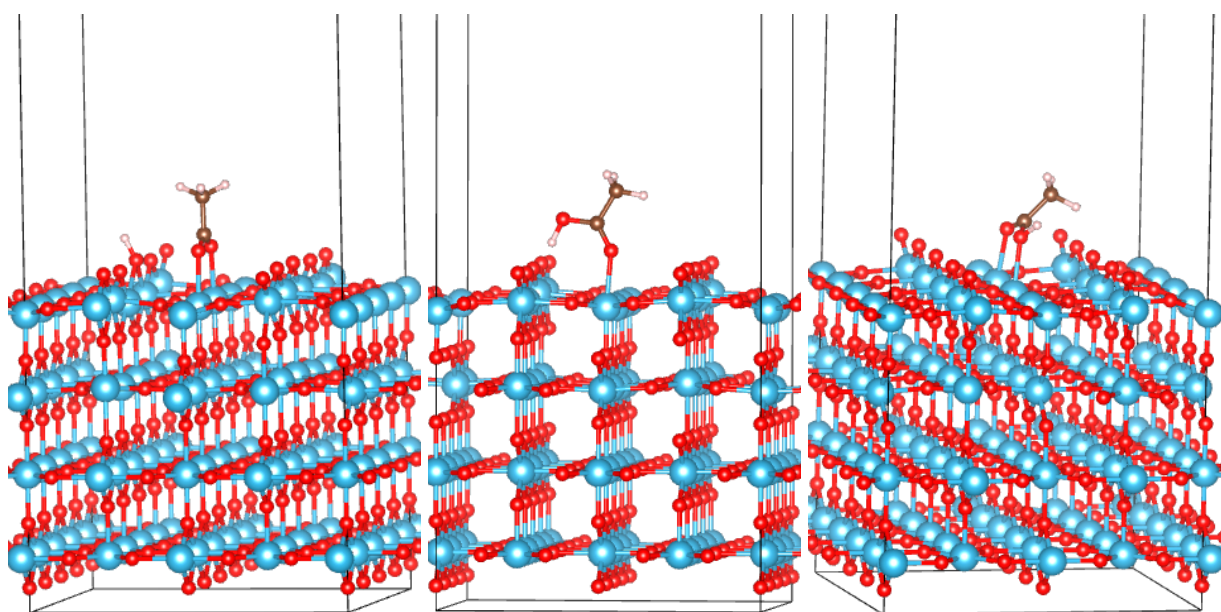


Figure 3. Adsorption configurations of AcOH on the rutile (110) surface of TiO_2 : BB (left), M1 (middle) and M2B (right).

(B) (001): Three bidentate (BB1 to BB3) and six monodentate configurations (M1 to M6) were identified and are shown in Figure 4. Their adsorption energies are listed in Table 1. BB1 and BB2 configurations, while visually similar, differ in that the COO group straddles different types of surface oxygen atoms, located in a slightly more “sagged” or slightly more protruding oxygen rows, respectively. This corresponds to significantly different E_{ads} (−0.74 and −0.41 eV, respectively). The strongest bound configuration ($E_{\text{ads}} = -1.11$ eV) is BB3, which straddles different Ti rows. In the BB configurations, both oxygen atoms of the carboxylic group bind to surface Ti atoms with both $O_{\text{mol-Ti}}$ bond lengths within 2.23–2.25 Å, with the shortest lengths corresponding to the strongest-bound BB3 configuration. In all monodentate configurations, the $O_{\text{mol-Ti}}$ bond length is 2.27 Å; the $H_{\text{mol-O}_{\text{surf}}}$ bonds are spread within 1.86–2.08 Å. Similar to anatase and rutile, molecular adsorption has no appreciable effect on the band structure regardless of the configuration (Figure 1; not all M configurations are shown to prevent clutter, but no configuration changed the DOS).

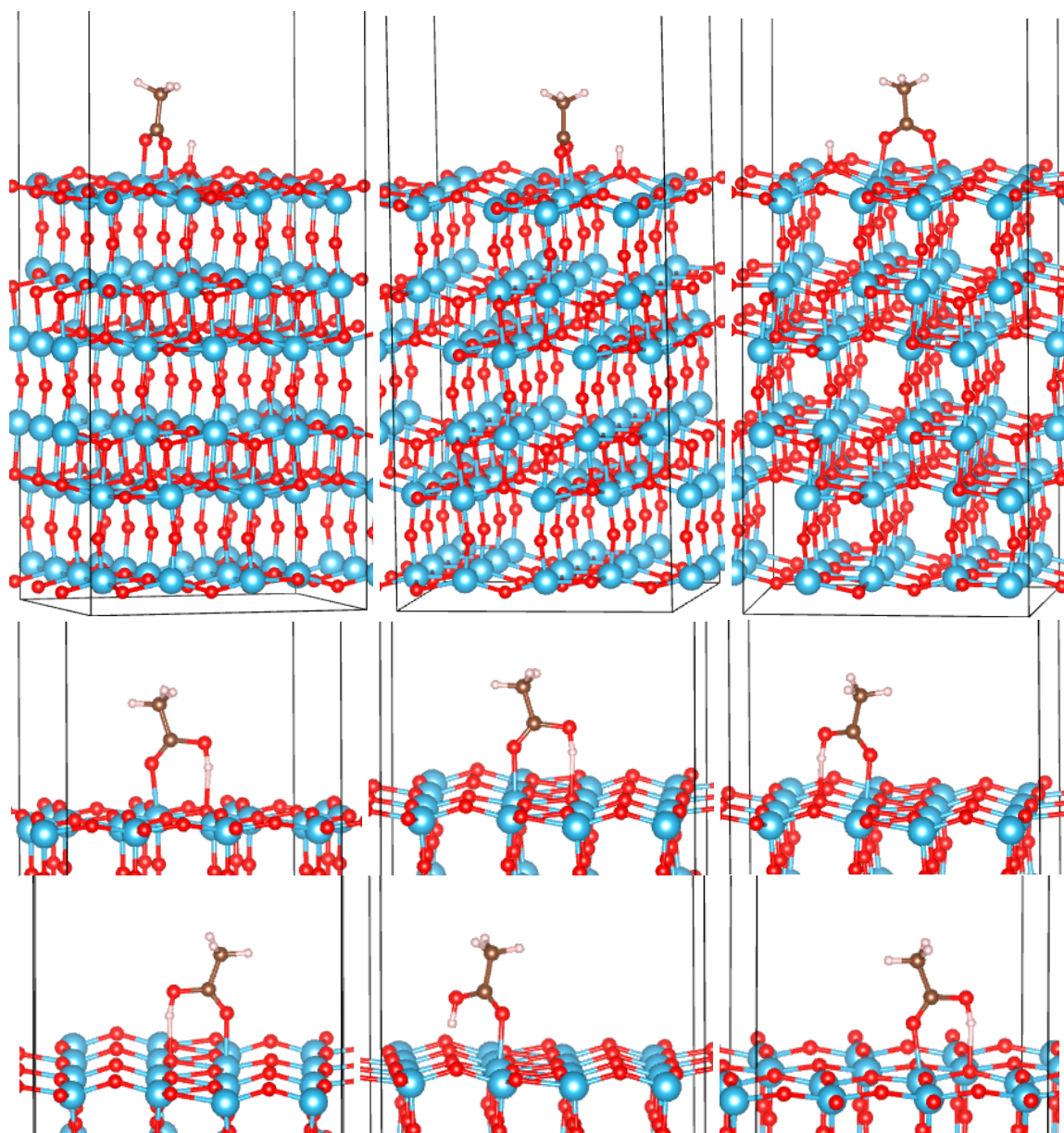


Figure 4. Adsorption configurations of AcOH on the (B) (001) surface of TiO₂. Top row: BB1 to BB3 (left to right). Bottom rows: M1 to M6 (left to right and top to bottom).

a-TiO₂: On both surfaces of *a*-TiO₂ (“top” and “bottom”), we have identified a total of six bidentate and nine monodentate configurations. They are shown in Figures 5 and 6, and their adsorption energies are listed in Table 1. While it is possible that other adsorption configurations exist on these surfaces, the 15 that we identified already provide an understanding of the strength of binding and the spread of adsorption energies on different sites of amorphous TiO₂. Similar to the crystalline surfaces, bidentate binding is energetically preferred. The O_{mol}-Ti bonds in BB configurations are generally shorter than on crystalline surfaces, the shortest reaching 1.91 Å (Table 1). While there is a dispersion of E_{ads} values among both monodentate and bidentate configurations, the strongest E_{ads} is larger than that of any crystalline surface in either the monodentate (reaching −1.83 eV) or bidentate (reaching −4.92 eV) regimes. Amorphous TiO₂ can therefore be used to achieve stable anchoring of organic molecules, such as dyes, that bind via a -COOH group.

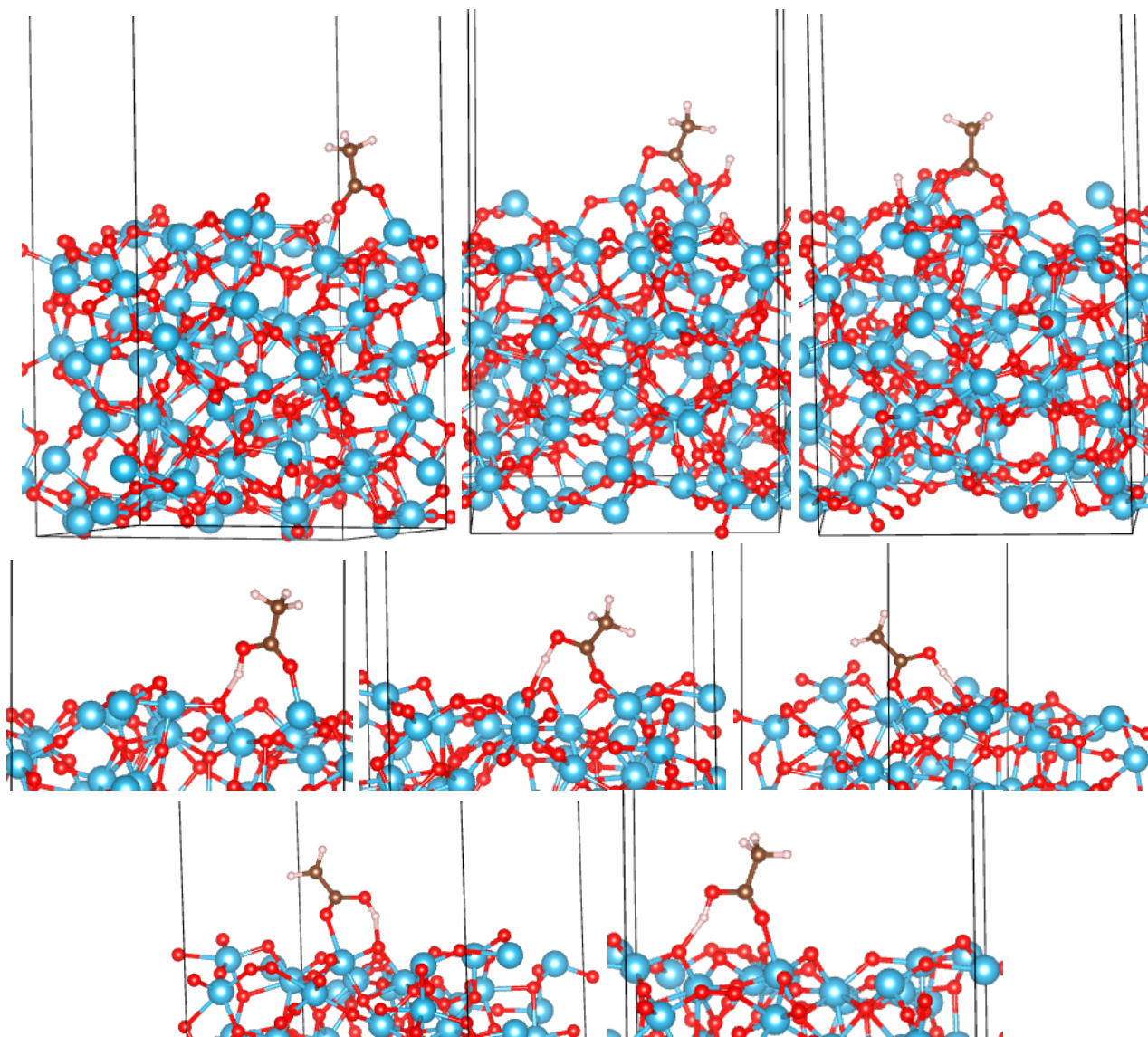


Figure 5. Adsorption configurations of AcOH on the “top” surface of α -TiO₂. Top row: BB1 to BB3 (left to right). Bottom rows: M1 to M5 (left to right and top to bottom).

3.3. Correlates of Adsorption Strength

On all surfaces, bidentate configurations are more strongly bound to the surface than monodentate, and from Table 1, it can be seen that increased binding strength generally corresponds to shorter molecule-surface distances and more positive charge on the molecule. In Figure 7, we quantify this dependence by plotting E_{ads} vs. the molecular charge q . Points corresponding to adsorption on amorphous surfaces are highlighted. There is a significant linear trend, with only two outlier points for bidentate and one outlier for monodentate configurations, with all outliers corresponding to α -TiO₂. This is not surprising given the expected differences of the chemical environments of the adsorbed molecule in different parts of an amorphous surface. Even so, the correlation is significant, with Pearson correlation coefficients (R^2) of 0.69 and 0.88 for bidentate and monodentate configurations, respectively. Figure 7 also highlights that E_{ads} in excess of -3 eV is only achieved in bidentate modes on α -TiO₂ and only with positive q values, in contrast with bidentate binding on crystalline surfaces,

where the molecule accepts charge (we note that the scales of q should not be directly compared for BB and M configurations, as in one case, H is dissociated and in the other, it is not; see Figures 2–6).

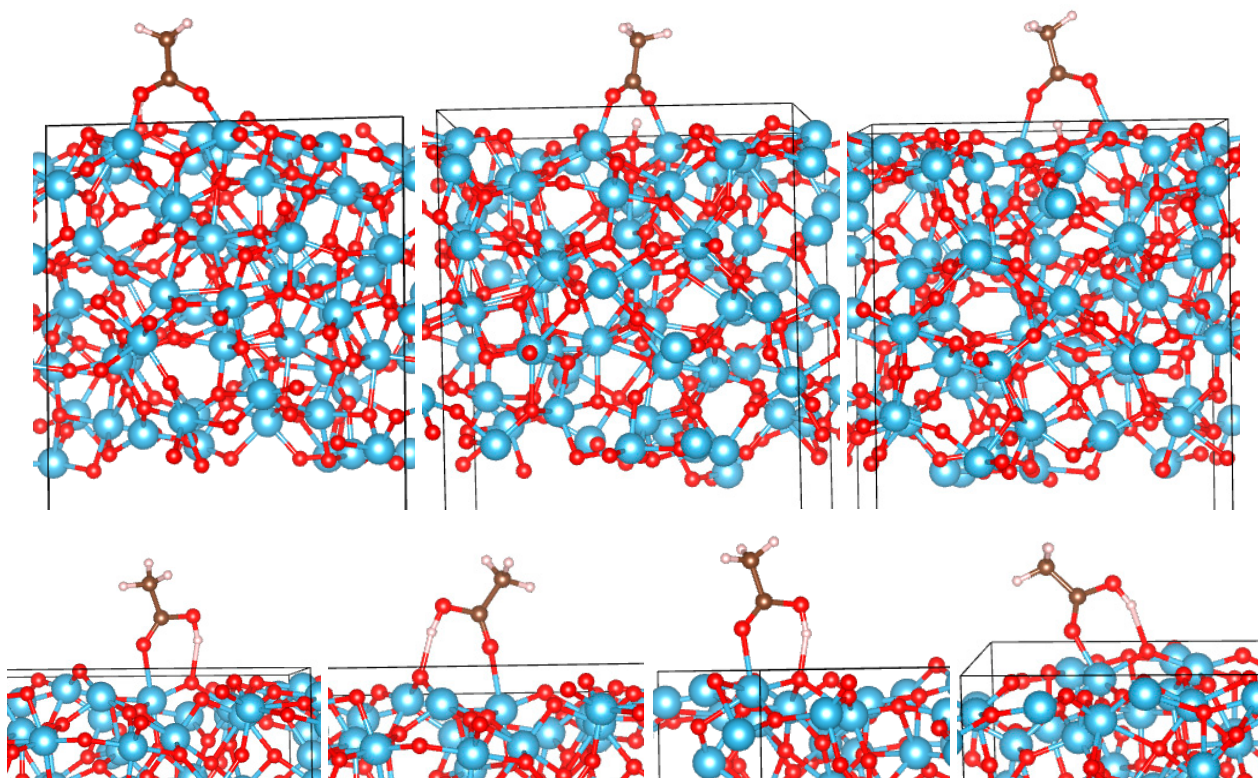


Figure 6. Adsorption configurations of AcOH on the “bottom” surface of α -TiO₂. Top row: BB1 to BB3 (left to right). Bottom row: M1 to M4 (left to right).

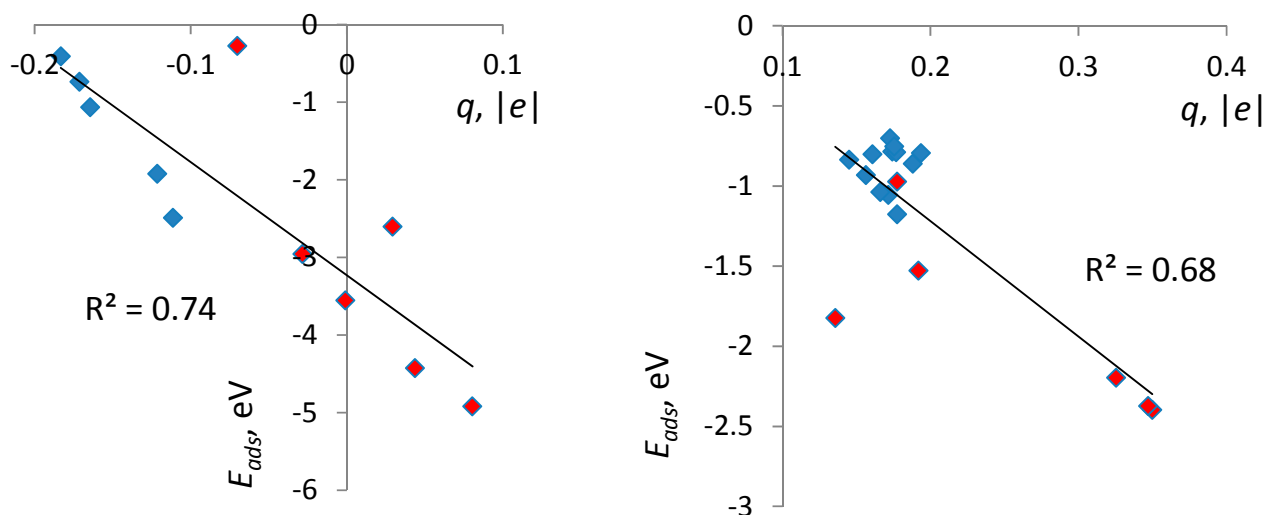


Figure 7. Dependence of the adsorption energy E_{ads} on the molecular charge q in bidentate (left) and monodentate (right) configurations on all surfaces and their linear regressions. Points corresponding to α -TiO₂ are highlighted in red.

Trends can also be identified between the adsorption energy and the shorter O_{mol} -Ti distance, with correlation coefficients (R^2) of 0.69 and 0.88 for bidentate and monodentate configurations, respectively. A combined linear regression in these two variables (*i.e.*, charge and bond length) unveils a significant

correlation with the correlation coefficient of 0.75 and 0.93 for bidentate and monodentate configurations, respectively.

4. Conclusions

We have presented the first comparative density functional tight binding study of acetic acid adsorption on anatase (101), rutile (110), B (001) and amorphous surfaces of TiO₂. On all surfaces, bidentate bridging adsorption configurations are preferred, consistent with available data. The computed adsorption energies of the lowest-energy bidentate configurations $E_{ads} = -1.93$, -2.49 and -1.09 eV on anatase, rutile and (B)-TiO₂, respectively. For monodentate configurations, the strongest $E_{ads} = -1.06$, -1.11 and -0.86 eV on anatase, rutile and (B)-TiO₂, respectively. The comparison with previously reported DFT values for E_{ads} computed with different computational setups highlights the need to use one and the same setup to obtain truly comparative values of E_{ads} among different phases and configurations.

Multiple monodentate and bidentate configurations are identified on α -TiO₂ with a distribution of adsorption energies and with the lowest binding energy stronger than that of the crystalline counterparts, with E_{ads} up to -4.92 eV for bidentate and -1.83 eV for monodentate adsorption. Amorphous TiO₂ can therefore be used to achieve strong anchoring of organic molecules, such as dyes, that bind via a -COOH group. While the presence of the surface leads to a contraction of the band gap vs. bulk, molecular adsorption caused no appreciable effect on the band structure around the gap in any of the systems.

Then, comparison among five surfaces (three crystalline and two amorphous) and a total of 30 binding geometries and energies allowed us to identify correlations between the binding strength, the charge donation at the interface and bond lengths between molecular and surface atoms. There is a strong positive correlation between the adsorption strength and the positive charge on the molecule, as well as between E_{ads} and the shortest bond length between molecular O and surface Ti atoms.

Acknowledgments

This work was supported by an AcRF Tier 1 grant by the Ministry of Education of Singapore (WBS R-265-000-494-112). S.M. thanks Fleur Legrain for technical assistance and Thomas Frauenheim and Balint Aradi, the University of Bremen, for the discussion about the DFTB method. K.Y. acknowledges the funding from the Ministry of Education, Culture, Sports, Science and Technology, Japan (MEXT).

Author Contributions

S.M. and G.G. did the calculations and wrote the text. S.M. conceived the project. K.Y. provided project guidance and input factors.

Conflicts of Interest

The authors declare no conflict of interest.

References

1. Sorescu, D.C.; Civiš, S.; Jordan, K.D. Mechanism of oxygen exchange between CO₂ and TiO₂(101) anatase. *J. Phys. Chem. C* **2014**, *118*, 1628–1639.
2. Müller, K.; Lu, D.; Senanayake S.D.; Starr, D.E. Monoethanolamine adsorption on TiO₂(110): Bonding, structure, and implications for use as a model solid-supported CO₂ capture material. *J. Phys. Chem. C* **2013**, *118*, 1576–1586.
3. Drew, K.; Girishkumar, G.; Vinodgopal, K.; Kamat, P.V. Boosting fuel cell performance with a semiconductor photocatalyst: TiO₂/Pt-Ru hybrid catalyst for methanol oxidation. *J. Phys. Chem. B* **2005**, *109*, 11851–11857.
4. Liu, Y.; Li, J.; Zhou, B.; Chen, H.; Wang, Z.; Cai, W. A TiO₂-nanotube-array-based photocatalytic fuel cell using refractory organic compounds as substrates for electricity generation. *Chem. Commun.* **2011**, *47*, 10314–10316.
5. Upadhyaya, H.M.; Senthilarasu, S.; Hsu, M.-H.; Kumar, D.K. Recent progress and the status of dye-sensitized solar cell (DSSC) technology with state-of-the-art conversion efficiencies. *Sol. Energy Mater. Sol. Cells* **2013**, *119*, 291–295.
6. Ning, Z.; Fu, Y.; Tian, H. Improvement of dye-sensitized solar cells: What we know and what we need to know. *Energy Environ. Sci.* **2010**, *3*, 1170–1181.
7. Jung, H.S.; Lee, J.-K. Dye sensitized solar cells for economically viable photovoltaic systems. *J. Phys. Chem. Lett.* **2013**, *4*, 1682–1693.
8. Hagfeldt, A.; Boschloo, G.; Sun, L.; Kloo, L.; Pettersson, H. Dye-sensitized solar cells. *Chem. Rev.* **2010**, *110*, 6595–6663.
9. Bai, Y.; Mora-Sero, I.; de Angelis, F.; Bisquert, J.; Wang, P. Titanium dioxide for photovoltaic applications. *Chem. Rev.* **2014**, *114*, 10095–10130.
10. Kojima, A.; Teshima, K.; Shirai, Y.; Miyasaka, T. Organometallic halide perovskites as visible-light sensitizers for photovoltaic cells. *J. Am. Chem. Soc.* **2009**, *131*, 6050–6051.
11. Kim, H.-S.; Lee, C.-R.; Im, J.-H.; Lee, K.-B.; Moehl, T.; Marchioro, A.; Moon, S.-J.; Humphry-Baker, R.; Yum, J.-H.; Moser, J.E.; *et al.* Lead iodide perovskite sensitized all-solid-state submicron thin film mesoscopic solar cell with efficiency exceeding 9%. *Sci. Rep.* **2012**, *2*, 591, doi:10.1038/srep00591.
12. Deng, D.; Kim, M.G.; Lee, J.Y.; Chi, J. Green energy storage materials: Nanostructured TiO₂ and Sn-based anodes for lithium-ion batteries. *Energy Environ. Sci.* **2009**, *2*, 818–837.
13. Yang, Z.; Choi, D.; Kerisit, S.; Rosso, K.M.; Wang, D.; Zhang, J.; Graff, G.; Liu, J. Nanostructures and lithium electrochemical reactivity of lithium titanites and titanium oxides: A review. *J. Power Sources* **2009**, *192*, 588–598.
14. Liu, S.; Hu, J.J.; Yan, N.F.; Pan, G.L.; Li, G.R.; Gao, X.P. Aluminum storage behavior of anatase TiO₂ nanotube arrays in aqueous solution for aluminum ion batteries. *Energy Environ. Sci.* **2012**, *5*, 9743–9746.
15. Dylla, A.G.; Henkelman, G.; Stevenson, K.J. Lithium insertion in nanostructured TiO₂(B) architectures. *Acc. Chem. Res.* **2013**, *46*, 1104–1112.

16. Myung, S.-T.; Kikuchi, M.; Yoon, C.S.; Yashiro, H.; Kim, S.-J.; Sun, Y.-K.; Scrosati, B. Black anatase titania enabling ultra high cycling rates for rechargeable lithium batteries. *Energy Environ. Sci.* **2013**, *6*, 2609–2614.
17. Li, W.; Wang, F.; Feng, S.; Wang, J.; Sun, Z.; Li, B.; Li, Y.; Yang, J.; Elzatahry, A.; Xia, Y.; *et al.* Sol–gel design strategy for ultradispersed TiO₂ nanoparticles on graphene for high-performance lithium ion batteries. *J. Am. Chem. Soc.* **2013**, *135*, 18300–18303.
18. Kim, K.-T.; Ali, G.; Chung, K.Y.; Yoon, C.S.; Yashiro, H.; Sun, Y.-K.; Lu, J.; Amine, K.; Myung, S.-T. Anatase titania nanorods as an intercalation anode material for rechargeable sodium batteries. *Nano Lett.* **2014**, *14*, 416–422.
19. Xu, H.; Zhang, R.Q.; Ng, A.M.C.; Djurisic, A.B.; Chan, H.T.; Chan, W.K.; Tong, S.Y. Splitting water on metal oxide surfaces. *J. Phys. Chem. C* **2011**, *115*, 19710–19715.
20. Xiang, G.; Wang, Y.-G.; Li, J.; Zhuang, J.; Wang, X. Surface-specific interaction by structure-match confined pure high-energy facet of unstable TiO₂(B) polymorph. *Sci. Rep.* **2013**, *3*, doi:10.1038/srep01411.
21. Niu, M.; Cheng, D.; Cao, D. Fluorite TiO₂(111) surface phase for enhanced visible-light solar energy conversion. *J. Phys. Chem. C* **2014**, *118*, 20107–20111.
22. Vittadini, A.; Casarin, M.; Selloni, A. Structure and stability of TiO₂-B surfaces: A Density Functional study. *J. Phys. Chem. C* **2009**, *113*, 18973–18977.
23. Perron, H.; Domain, C.; Roques, J.; Drot, R.; Simoni, E.; Catalette, H. Optimisation of accurate rutile TiO₂ (110), (100), (101) and (001) surface models from periodic DFT calculations. *Theor. Chem. Acc.* **2007**, *117*, 565–574.
24. Giorgi, G.; Fujisawa, J.-I.; Segawa, H.; Yamashita, K. Unraveling the adsorption mechanism of aromatic and aliphatic diols on TiO₂ surface: a density functional theory analysis. *Phys. Chem. Chem. Phys.* **2013**, *15*, 9761–9767.
25. Heckel, W.; Elsner, B.A.M.; Schulz, C.; Müller, S. The role of hydrogen on the adsorption behavior of carboxylic acid on TiO₂ surfaces. *J. Phys. Chem. C* **2014**, *118*, 10771–10779.
26. Manzhos, S.; Segawa, H.; Yamashita, K. The effect of ligand substitution and water co-adsorption on the adsorption dynamics and energy level matching of amino-phenyl acid dyes on TiO₂. *Phys. Chem. Chem. Phys.* **2012**, *14*, 1749–1755.
27. O’Rourke, C.; Bowler, D.R. Adsorption of thiophene-conjugated sensitizers on TiO₂ anatase (101). *J. Phys. Chem. C* **2010**, *114*, 20240–20248.
28. Pastore, M.; de Angelis, F. Aggregation of organic dyes on TiO₂ in dye-sensitized solar cells models: an *ab initio* investigation. *ACS Nano* **2010**, *4*, 556–562.
29. De Angelis, F.; Fantacci, S.; Gebauer, R. Simulating dye-sensitized TiO₂ heterointerfaces in explicit solvent: Absorption spectra, energy levels, and dye desorption. *J. Phys. Chem. Lett.* **2011**, *2*, 813–817.
30. Spreafico, C.; Schiffmann, F.; VandeVondele, J. Structure and mobility of acetic acid at the anatase (101)/acetonitrile interface. *J. Phys. Chem. C* **2014**, *118*, 6251–6260.
31. Anselmi, C.; Mosconi, E.; Pastore, M.; Ronca, E.; de Angelis, F. Adsorption of organic dyes on TiO₂ surfaces in dye-sensitized solar cells: interplay of theory and experiment. *Phys. Chem. Chem. Phys.* **2012**, *14*, 15963–15974.

32. Vittadini, A.; Selloni, A.; Rotzinger, F.P.; Graitzel, M. Formic acid adsorption on dry and hydrated TiO₂ Anatase (101) surfaces by DFT calculations. *J. Phys. Chem. B* **2000**, *104*, 1300–1306.
33. Agosta, L.; Zollo, G.; Arcangeli, C.; Buonocore, F.; Gala, F.; Celino, M. Water driven adsorption of amino acids on the (101) anatase TiO₂ surface: An *ab initio* study. *Phys. Chem. Chem. Phys.* **2015**, *17*, 1556–1561.
34. Coropceanu V.; Cornil, J.; da Silva Filho, D.A.; Olivier, Y.; Silbey, R.; Brédas, J.L. Charge transport in organic semiconductors. *Chem. Rev.* **2007**, *107*, 926–952.
35. Borghols, W.J.H.; Wagemaker, M.; Lafont, U.; Kelder, E.M.; Mulder, F.M. Impact of nanosizing on lithiated rutile TiO₂. *Chem. Mater.* **2008**, *20*, 2949–2955.
36. Armstrong, A.R.; Arrouvel, C.; Gentili, V.; Parker, S.C.; Saiful Islam, M.; Bruce, P. Lithium coordination sites in Li_xTiO₂(B): A structural and computational study. *Chem. Mater.* **2010**, *22*, 6426–6432.
37. Borghols, W.J.H.; Lützenkirchen-Hecht, D.; Haake, U.; van Eck, E.R.H.; Muldera, F.M.; Wagemaker, M. The electronic structure and ionic diffusion of nanoscale LiTiO₂ anatase. *Phys. Chem. Chem. Phys.* **2009**, *11*, 5742–5748.
38. Kang, J.; Wei, S.-H.; Kim, Y.-H. First-principles theory of electrochemical capacitance of nanostructured materials: Dipole-assisted subsurface intercalation of lithium in pseudocapacitive TiO₂ anatase nanosheets. *J. Phys. Chem. C* **2011**, *115*, 4909–4915.
39. Sushko, M.L.; Rosso, K.M.; Liu, J. Mechanism of Li⁺/electron conductivity in rutile and anatase TiO₂ nanoparticles. *J. Phys. Chem. C* **2010**, *114*, 20277–20283.
40. Eithiraj, R.D.; Geethalakshmi, K.R. Suitability of amorphous TiO₂ nanoparticles as a photoelectrode in dye sensitized solar cells: A DFT–TDDFT study. *Chem. Phys. Lett.* **2013**, *585*, 138–142.
41. Tang, X.; Liu, X.; Zhang, L.; Xing, Y.; Tian, Y. Low crystallinity TiO₂ film with inherent low oxygen vacancy for sensitized solar cells. *Chem. Phys.* **2014**, *441*, 121–127.
42. Kakuta, N.; Oku, T.; Suzuki, A.; Kikuchi, K.; Kikuchi, S. Effect of an amorphous TiO₂ addition on dye-sensitized solar cells with organic dyes. *J. Ceram. Process. Res.* **2012**, *13*, 28–31.
43. Xiong, H.; Slater, M.D.; Balasubramanian, M.; Johnson, C.S.; Rajh, T. Amorphous TiO₂ nanotube anode for rechargeable sodium ion batteries. *J. Phys. Chem. Lett.* **2011**, *2*, 2560–2565.
44. Borghols, W.J.H.; Lützenkirchen-Hecht, D.; Haake, U.; Chan, W.; Lafont, U.; Kelder, E.M.; van Eck, E.R.H.; Kentgens, A.P.M.; Mulder, F.M.; Wagemaker, M. Lithium storage in amorphous TiO₂ nanoparticles. *J. Electrochem. Soc.* **2010**, *157*, A582–A588.
45. Hibino, M.; Abe, K.; Mochizuki, M.; Miyayama, M. Amorphous titanium oxide electrode for high-rate discharge and charge. *J. Power Sources* **2004**, *126*, 139–143.
46. Sun, X.; Xie, M.; Travis, J.J.; Wang, G.; Sun, H.; Lian, J.; George, S.M. Pseudocapitance of amorphous TiO₂ thin films anchored to graphene and carbon nanotubes using atomic layer deposition. *J. Phys. Chem. C* **2013**, *117*, 22497–22508.
47. Hai-Tao, F.; Min, L.; Da-Wei, W.; Tao, S.; Dong-Sheng, G.; Feng, L.; Jigang, Z.; Tsun-Kong, S.; Hui-Ming, C. Comparison of the rate capability of nanostructured amorphous and anatase TiO₂ for lithium insertion using anodic TiO₂ nanotube arrays. *Nanotechnology* **2009**, *20*, doi:10.1088/0957-4484/20/22/225701.

48. Yildirim, H.; Greeley, J.P.; Sankaranarayanan, S.K.R.S. Localized order–disorder transitions induced by Li segregation in amorphous TiO₂ nanoparticles. *ACS Appl. Mater. Interfaces* **2014**, *6*, 18962–18970.
49. Kaur, K.; Singh, C.V. Amorphous TiO₂ as a photocatalyst for hydrogen production: A DFT study of structural and electronic properties. *Energy Procedia* **2012**, *29*, 291–299.
50. Legrain, F.; Malyi, O.; Manzhos, S. Insertion energetics of lithium, sodium, and magnesium in crystalline and amorphous titanium dioxide: A comparative first-principles study. *J. Power Sources* **2015**, *278*, 197–202.
51. Legrain, F.; Malyi, O.; Manzhos, S. Comparative *ab initio* study of lithium storage in amorphous and crystalline TiO₂. In Proceedings of the 14th Asian Conference on Solid State Ionics, Singapore, Singapore, 24–27 June 2014.
52. Prasai, B.; Cai, B.; Underwood, M.K.; Lewis, J.P.; Drabold, D.A. Properties of amorphous and crystalline titanium dioxide from first principles. *J. Mater. Sci.* **2012**, *47*, 7515–7521.
53. Dolgonos, G. Self-consistent-charge density-functional tight-binding molecular dynamics simulations of amorphous TiO₂ growth. *Surf. Sci.* **2014**, *621*, 51–54.
54. Elstner, M.; Porezag, D.; Jungnickel, G.; Elsner, J.; Haugk, M.; Frauenheim, T.; Suhai, S.; Seifert, G. Self-consistent-charge density-functional tight-binding method for simulations of complex materials properties. *Phys. Rev. B* **1998**, *58*, 7260–7268.
55. Aradi, B.; Hourahine, B.; Frauenheim, T. DFTB+, a sparse matrix-based implementation of the DFTB method. *J. Phys. Chem. A* **2007**, *111*, 5678–5684.
56. Gemming, S.; Enyashin, A.; Frenzel, J.; Seifert, G. Adsorption of nucleotides on the rutile (110) surface. *Int. J. Mater. Res.* **2010**, *101*, 758–764.
57. Zhu, T.; Gao, S.-P. The stability, electronic structure, and optical property of TiO₂ polymorphs. *J. Phys. Chem. C* **2014**, *118*, 11385–11396.
58. Burdett, J.K.; Hughbanks, T.; Miller, G.J.; Richardson, J.W.; Smith, J.V. Structural-electronic relationships in inorganic solids: Powder neutron diffraction studies of the rutile and anatase polymorphs of titanium dioxide at 15 and 295 K. *J. Am. Chem. Soc.* **1987**, *109*, 3639–3646.
59. Horn, M.; Schwerdtfeger, C.F.; Meagher, E.P. Refinement of the structure of anatase at several temperatures. *Z. Kristallogr.* **1972**, *136*, 273–281.
60. Asahi, R.; Taga, Y.; Mannstadt, W.; Freeman, A.J. Electronic and optical properties of anatase TiO₂. *Phys. Rev. B* **2000**, *61*, 7459–7465.
61. Labat, F.; Baranek, P.; Domain, C.; Minot, C.; Adamo, C. Density functional theory analysis of the structural and electronic properties of TiO₂ rutile and anatase polytypes: Performances of different exchange-correlation functionals. *J. Chem. Phys.* **2007**, *126*, 154703–12.
62. Tang, H.; Berger, H.; Schmid, P.E.; Lévy, F.; Burri, G. Photoluminescence in TiO₂ anatase single crystals. *Solid State Commun.* **1993**, *87*, 847–850.
63. Dolgonos, G.; Aradi, B.; Moreira, N.H.; Frauenheim, T. An improved self-consistent-charge Density-Functional Tight-Binding (SCC-DFTB) set of parameters for simulation of bulk and molecular systems involving titanium. *J. Chem. Theory Comput.* **2010**, *6*, 266–278.
64. Tezuka, Y.; Shin, S.; Lshii, T.; Ejima, T.; Suzuki, S.; Sato, S. Photoemission and Bremsstrahlung Isochromat spectroscopy studies of TiO₂ (Rutile) and SrTiO₃. *J. Phys. Soc. Jpn.* **1994**, *63*, 347–357.

65. Pascual, J.; Camassel, J.; Mathieu, H. Resolved quadrupolar transition in TiO₂. *Phys. Rev. Lett.* **1977**, *39*, 1490–1493.
66. Pascual, J.; Camassel, J.; Mathieu, H. Fine structure in the intrinsic absorption edge of TiO₂. *Phys. Rev. B* **1978**, *18*, 5606–5614.
67. *CRC Handbook of Chemistry and Physics*, 67th ed.; CRC: Cleveland, OH, USA, 1986.
68. Chase, M.W.; Davies, C.A.; Downey, J.R.; Frurip, D.J.; McDonald, R.A.; Syverud, A.N. JANAF Thermodynamical Tables, 3rd ed. *J. Phys. Chem. Ref. Data* **1985**, *14* (Suppl. 1), 1680.
69. Hamad, B.A. First-principle calculations of structural and electronic properties of rutile-phase dioxides (MO₂), M = Ti, V, Ru, Ir and Sn. *Eur. Phys. J. B* **2009**, *70*, 163–169.
70. Lazzeri, M.; Vittadini, A.; Selloni, A. Structure and energetics of stoichiometric TiO₂ anatase surfaces. *Phys. Rev. B* **2001**, *63*, 155409.
71. Yang, H.G.; Sun, C.H.; Qiao, S.Z.; Zou, J.; Liu, G.; Smith, S.C.; Cheng, H.M.; Lu, G.Q. Anatase TiO₂ single crystals with a large percentage of reactive facets. *Nature* **2008**, *453*, 638–641.
72. Yahia, M.B.; Lemoigno, F.; Beuvier, T.; Filhol, J.-S.; Richard-Plouet, M.; Brohan, L.; Doublet, M.-L. Updated references for the structural, electronic, and vibrational properties of TiO₂(B) bulk using first-principles density functional theory calculations. *J. Chem. Phys.* **2009**, *130*, 204501–204511.
73. Betz, G.; Tributsch, H.; Marchand, R. Hydrogen insertion (intercalation) and light induced proton exchange at TiO₂(B) -electrodes. *J. Appl. Electrochem.* **1984**, *14*, 315–322.
74. Kresse, G.; Hafner, J. Ab initio molecular dynamics for liquid metals. *Phys. Rev. B* **1993**, *47*, 558.
75. Kresse, G.; Hafner, J. Ab initio molecular-dynamics simulation of the liquid-metal-amorphous-semiconductor transition in germanium. *Phys. Rev. B: Condens. Matter.* **1994**, *49*, 14251–14269.
76. Kresse, G.; Furthmüller, J. Efficiency of ab-initio total energy calculations for metals and semiconductors using a plane-wave basis set. *Comput. Mat. Sci.* **1996**, *6*, 15–50.
77. Kresse, G.; Furthmüller, J. Efficient iterative schemes for ab initio total-energy calculations using a plane-wave basis set. *Phys. Rev. B* **1996**, *54*, 11169.
78. Perdew, J.P.; Burke, K.; Ernzerhoff, M. Generalized gradient approximation made simple. *Phys. Rev. Lett.* **1996**, *77*, 3865–3868.
79. Blochl, P.E. Projector augmented-wave method. *Phys. Rev. B* **1994**, *50*, 17953–17978.
80. Chan, M.; Carrington, T.; Manzhos, S. Anharmonic vibrations of the carboxyl group in acetic acid on TiO₂: implications for adsorption mode assignment in dye-sensitized solar cells. *Phys. Chem. Chem. Phys.* **2013**, *15*, 10028–10034.
81. Soler, J.M.; Artacho, E.; Dale, J.D.; Garcia, A.; Junquera, J.; Ordejon, P.; Sanchez-Portal, D. The SIESTA method for *ab initio* order-*N* materials simulation. *J. Phys.: Condens. Matter* **2002**, *14*, 2745–2779.
82. Troullier, N.; Martins, J.L. Efficient pseudopotentials for plane-wave calculations. *Phys. Rev. B* **1991**, *43*, 1993–2006.
83. Hutter, J.; Iannuzzi, M.; Schiffmann, F.; VandeVondele, J. CP2K: Atomistic simulations of condensed matter systems. *WIREs Comput. Mol. Sci.* **2014**, *4*, 15–25.
84. Hartwigsen, C.; Goedecker, S.; Hutter, J. Relativistic separable dual-space Gaussian pseudopotentials from H to Rn. *Phys. Rev. B* **1998**, *58*, 3641–3662.

85. Lippert, G.; Hutter, J.; Parrinello, M. A hybrid Gaussian and plane wave Density Functional scheme. *Mol. Phys.* **1997**, *92*, 477–487.
86. Grimme, S.; Antony, J.; Ehrlich, S.; Krieg, H. A consistent and accurate *ab initio* parametrization of density functional dispersion correction (DFT-D) for the 94 elements H-Pu. *J. Chem. Phys.* **2010**, *132*, 154104.
87. Momma, K.; Izumi, F. VESTA 3 for three-dimensional visualization of crystal, volumetric and morphology data. *J. Appl. Crystallogr.* **2011**, *44*, 1272–1276.
88. Tao, J.; Luttrell, T.; Bylsma, J.; Batzill, M. Adsorption of acetic acid on rutile TiO₂(110) vs. (011)-2 × 1 surfaces. *J. Phys. Chem. C* **2011**, *115*, 3434–3442.
89. Diebold, U. The surface science of titanium dioxide. *Surf. Sci. Rep.* **2003**, *48*, 53–229.

© 2015 by the authors; licensee MDPI, Basel, Switzerland. This article is an open access article distributed under the terms and conditions of the Creative Commons Attribution license (<http://creativecommons.org/licenses/by/4.0/>).